CrossMark
click for updates

High-performance printable hybrid perovskite solar cells with an easily accessible n-doped fullerene as a cathode interfacial layer†

Chih-Yu Chang,*[a] Bo-Chou Tsai,[a] Yu-Cheng Hsiao,[a] Yu-Ching Huang[b] and Cheng-Si Tsao[bc]

Engineering the interface between the active layer and the electrodes has proven to be a promising strategy to enhance the power conversion efficiency (PCE) of hybrid perovskite solar cells (PeSCs). Here, we present an effective approach to achieve highly efficient PeSCs by inserting an easy-accessible hexamethonium bromide (HMB)-doped [6,6]-phenyl-C_{61}-butyric acid methyl ester ($PC_{61}BM$) film between the active perovskite layer and the Ag cathode. This doped interfacial layer delivers several remarkable features for use in PeSCs, including solution processability, good electrical conductivity, fine work-function tunability of the Ag electrode, and general applicability to different fullerene materials. As a consequence, planar-heterojunction PeSCs deliver a PCE up to ~18%, showing an approximately 5.6-fold enhancement compared with the control device using an undoped $PC_{61}BM$ layer. In particular, benefitting from the high conductivity of this doped film, a prominent PCE as high as 15.58% can be achieved even when a large thickness of the $PC_{61}BM$ layer (120 nm) is used. To the best of our knowledge, this is the highest performance ever reported for PeSCs with a $PC_{61}BM$ thickness more than 100 nm. More encouragingly, large-area PeSCs (active area = 1.2 cm^2) *via* the doctor-blade coating technique also exhibit a remarkable PCE (15.23%) and good long-term stability under an inert atmosphere. Our results indicate that the HMB-doped $PC_{61}BM$ film is a promising interfacial layer for PeSCs and can be compatible with high throughput roll-to-roll manufacturing processes.

Introduction

Hybrid organic–inorganic lead halide perovskite solar cells (PeSCs) have been considered one of the most promising next generation photovoltaic technologies due to their reasonable device performance, cost-effective manufacturing, light weight, and mechanical flexibility.[1–4] Over the past few years, significant progress in developing new perovskite materials and improving the morphology of perovskite layers has led to the rapid improvement of power conversion efficiency (PCE) to up to 21% on lab-scale devices.[2–5] In addition to the optimization of the perovskite active layer, the interfacial layers that are in contact with both the perovskite layer and the electrodes should also be engineered to achieve high device performance.[4–9] Ideally, the work-function (WF) of the electrode must be well-matched to

the energy level of the active layer to achieve an Ohmic contact, which can maximize achievable open-circuit voltage (V_{oc}) and minimize the resistance for charge extraction.[5,8,9]

For typical planar heterojunction PeSCs, the perovskite layer is sandwiched between a hole transport layer (HTL) and an electron transport layer (ETL) that are in contact with their corresponding electrodes. Based on the direction of charge flow, the device architecture can be categorized into the p–i–n and n–i–p configurations.[4,5] Compared to the n–i–p configuration, the p–i–n configuration (substrate/anode/HTL/perovskite/ ETL/ cathode) has drawn much attention owing to its low processing temperature, negligible hysteresis in current–voltage characteristics, and great potential applications in flexible devices.[5,10] A commonly used device structure for the p–i–n configuration comprises glass substrate/indium tin oxide (ITO)/ poly(3,4-ethylenedioxythiophene):poly(styrenesulfonate)(PEDOT: PSS)/perovskite/fullerene/cathode.[5] Despite several advantages, the p–i–n type devices generally suffer from poor ambient stability due mainly to the use of highly reactive low WF metals (*e.g.* Al or Ca) as the cathode.[11,12] To circumvent this problem, one can replace the low WF metals with environmental-stable high WF metals (*e.g.* Ag or Au). This approach, however, often compromises

[a] *Department of Materials Science and Engineering, Feng Chia University, Taichung, Taiwan 40724, Republic of China. E-mail: changcyu@fcu.edu.tw*

[b] *Institute of Nuclear Energy Research, Longtan, Taoyuan, Taiwan 32546, Republic of China*

[c] *Department of Materials Science and Engineering, National Taiwan University, Taipei, Taiwan 10617, Republic of China*

31836 | *Phys. Chem. Chem. Phys.,* 2016, **18**, 31836–31844

This journal is © the Owner Societies 2016

the device performance because of the mismatch between the WF of these metals and the lowest unoccupied molecular orbital (LUMO) level of $PC_{61}BM$ (~ 4.2 eV).[8,13–20] It is thus highly desirable to insert a cathode buffer layer (CBL) to achieve appropriate energy level matching at the $PC_{61}BM$/cathode interface. Several materials such as metal oxides and cationic quaternary ammonium-based molecules have been used as the CBLs to reduce the WF of the electrode for more efficient electron extraction.[5,8,9,13–21] The inclusion of these CBLs, however, can certainly increase the fabrication complexity and reduce the reproducibility due to the requirements of additional deposition steps and accurate control of the CBL film thickness.

Apart from the incorporation of additional CBLs, doping $PC_{61}BM$ with an appropriate dopant to form an n-doped layer has been demonstrated as an effective strategy for achieving high-performance PeSCs with a high WF metal cathode.[18,22] This n-doped $PC_{61}BM$ layer is capable of serving as both a CBL and an ETL, thus simplifying the manufacturing process. For example, we have recently demonstrated that the incorporation of tetra-alkyl ammonium bromides as n-type dopants into the $PC_{61}BM$ layer is a very promising approach to achieve highly efficient and stable PeSCs.[18] Due to the superior conductivity of this n-doped $PC_{61}BM$, a wide range of film thicknesses can be applied to produce high performance devices, which is beneficial for the fabrication of PeSCs using high throughput printing techniques (e.g. blade coating).[18] Despite these advances, a similar concept has rarely been applied to PeSCs so far. In addition, from a molecular point of view, the long cetyl alkyl chain (C16) on this dopant will inevitably enlarge the insulating effects, which in turn impedes the charge transport properties of the doped film. It is thus highly desirable to utilize other dopants with shorter alkyl chains.

In this study, we report a simple and effective strategy to improve the performance of PeSCs through the incorporation of a commercially available solution-processed hexamethonium bromide (HMB)-doped [6,6]-phenyl-C_{61}-butyric acid methyl ester ($PC_{61}BM$) film as a cathode interfacial layer (see Fig. 1a for the device structure and the chemical structures). Our results indicate that HMB with a short alkyl chain length (C6) acts as an effective n-dopant, which can drastically improve the electrical conductivity of the $PC_{61}BM$ film by more than five orders of magnitude. In particular, the high conductivity ($\sim 6.5 \times 10^{-3}$ S cm^{-1}) of this doped film makes it capable of functioning as an efficient interfacial layer in a wide thickness range of 60 to 120 nm. In addition to the improved film conductivity, the quaternary ammonium cations of HMB endow the formation of favorable interfacial dipoles to turn a high-WF Ag electrode into an efficient low-WF electrode. These characteristics enable this doped $PC_{61}BM$ film to function as both an ETL and a CBL, thereby simplifying the manufacturing processes of the devices. With this doped interfacial layer, the resulting device delivers a PCE up to 17.96%, which is much superior to that of the control device with an undoped $PC_{61}BM$ layer (maximum PCE = 3.23%). In particular, a prominent PCE as high as 15.58% is also achieved for the device with a 120 nm thick $PC_{61}BM$ layer, which represents the highest efficiency ever reported for PeSCs with a $PC_{61}BM$ film thickness more than 100 nm. More significantly, the applicability of this doped layer to large-area PeSCs (active area = 1.2 cm^2) fabricated by scalable doctor-blade coating is also demonstrated, yielding
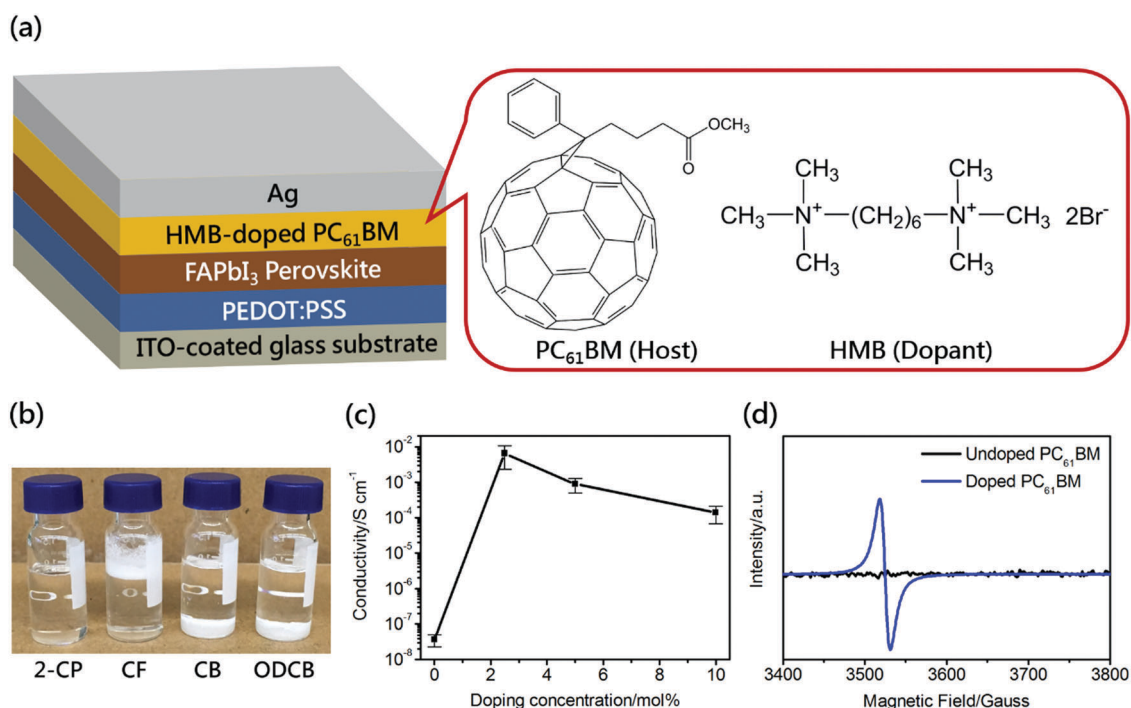

Fig. 1 (a) Schematic illustration of the device architecture used in this study and the chemical structures of $PC_{61}BM$ and HMB. (b) Photographic image of HMB in various solvents (1.0 wt%) at room temperature. (c) Conductivities of HMB-doped $PC_{61}BM$ films at varying dopant concentrations. (d) EPR spectra of the undoped $PC_{61}BM$ and doped $PC_{61}BM$ films.

This journal is © the Owner Societies 2016

Phys. Chem. Chem. Phys., 2016, **18**, 31836–31844 | **31837**

high device performance (PCE up to 15.23%) and good long-term stability under an inert atmosphere. The present findings highlight the feasibility of using HMB-doped $PC_{61}BM$ as an effective cathode interfacial layer for PeSCs and provide valuable insights into the development of highly efficient PeSCs based on large-scale manufacturing methods.

Results and discussion

The selection of an appropriate solvent to ensure that both the $PC_{61}BM$ host and the HMB dopant are adequately dissolved is an important prerequisite for the construction of solution-processed PeSCs. We first attempt to examine the solubility of the HMB dopant in some chlorinated solvents (chloroform (CF), chlorobenzene (CB), ortho-dichlorobenzene (ODCB), and 2-chlorophenol (2-CP)) that are commonly used to dissolve fullerene derivatives. In contrast to cationic molecules with a sufficiently long alkyl chain, which are highly soluble in these organic solvents, HMB is found to be hardly soluble in CF, CB and DCB even at a low concentration of 1.0 wt%, leading to heterogeneous mixtures (Fig. 1b). In contrast, sufficiently high solubility (>30 mg mL^{-1}) of HMB was observed in the case of 2-CP solvent (Fig. 1b). It should be noted that 2-CP is also an orthogonal solvent to the lead halide perovskite film, which enables the fabrication of multilayer structures without the intermixing problem.

The electrical conductivities of $PC_{61}BM$ films at varying dopant concentrations were then studied using a four-point probe technique. Notably, the conductivity can be enhanced by more than five orders of magnitude upon doping with HMB. As shown in Fig. 1c, the conductivity increased from 5.1×10^{-8} S cm^{-1} (without doping) to a maximum of 1.1×10^{-2} S cm^{-1} (5 mol% doping), which is much higher than those of the other organic conducting materials such as PEDOT:PSS ($\sim 10^{-3}$ S cm^{-1} for Clevios P AI4083) and anionic conjugated polyelectrolytes ($\sim 1.5 \times 10^{-3}$ S cm^{-1}).[23,24] This enhancement in electrical conductivity is consistent with previous studies revealing that the incorporation of halide anions into $PC_{61}BM$ can induce effective n-doping via anion-induced electron transfer and thereby substantially increase film conductivity.[25,26] To confirm that anion-induced electron transfer indeed takes place in our system, the electron paramagnetic resonance (EPR) spectra of $PC_{61}BM$ films with and without adding 5 mol% dopant were recorded. As shown in Fig. 1d, the undoped film exhibited no appreciable paramagnetic signal, indicating its semiconducting nature. In contrast, the doped film revealed a strong paramagnetic signal, suggesting the formation of fullerene radical anions. When the doping concentrations were further increased to 10 mol%, however, the conductivity decreased obviously (Fig. 1c). This deterioration can be attributed to the tendency of excess HMB-caused molecular aggregation, as discussed below.

To gain more insight into the effect of HMB doping on the morphological alteration of the $PC_{61}BM$-coated perovskite layer, atomic force microscopy (AFM) measurements were performed in tapping mode (scan size = 5 μm × 5 μm). The FAPbI$_3$

perovskite film is prepared by two-step sequential solution deposition, and its detailed characterization can be found in our previous studies.[18,20,27] For the pristine FAPbI$_3$ perovskite film without the $PC_{61}BM$ capping layer, an inhomogeneous surface morphology with high root-mean-square (rms) roughness (~ 31.2 nm) was observed (ESI,† Fig. S1). The introduction of the undoped $PC_{61}BM$ layer into the perovskite layer, however, still exhibited microscale voids with an rms roughness of 4.1 nm (Fig. 2). It should be noted that the contrast of the AFM phase image is directly dependent on the composition and microphase separation of the samples. Considering that the 0 mol% doping sample (i.e. pure $PC_{61}BM$ film) should reveal uniform composition without phase separation, therefore, it is expected that a featureless phase image will be manifested (Fig. 2). Obviously, the introduction of the HMB dopant can effectively improve the coverage of the $PC_{61}BM$ film onto the perovskite layer. For the film with a doping concentration of 2.5 and 5 mol%, a relatively smooth surface (rms roughness <2.5 nm) with no obvious phase separation was observed (Fig. 2). This result may be associated with strong coulombic interaction between the $PC_{61}BM$ radical anion and alkylammonium cations, which can increase the solution viscosity and consequently facilitate $PC_{61}BM$ film coverage on the perovskite layer. A further increase in the doping concentration of HMB to 10 mol%, however, revealed a greater surface roughness (rms roughness = 4.5 nm) with more pronounced phase-separated domains (Fig. 2), which can impede charge transport between neighboring domains. These results correlated well with the trend observed in electrical conductivity measurements (Fig. 1c). It is worth noting that the complete coverage of the HMB-doped $PC_{61}BM$ film on the perovskite layer can ensure efficient charge transfer at the interface, which is highly desirable to realize high performance PeSCs (as will be discussed later).

The efficiency of charge transfer at the perovskite/$PC_{61}BM$ interface was examined by photoluminescence (PL) measurements. The PL properties of the pristine sample (i.e. glass substrate/PEDOT:PSS/FAPbI$_3$) and the samples coated with undoped and doped $PC_{61}BM$ films (doping concentration = 10 mol%) were investigated under excitation at a wavelength of 530 nm. The steady-state PL spectra of the studied samples are shown in Fig. 3a. For the pristine FAPbI$_3$ sample, a clear emission peak centered at ~ 820 nm was observed, which originated from the radiative recombination of photogenerated charge carriers in the FAPbI$_3$ film. When the FAPbI$_3$ perovskite layer formed a contact with either an undoped $PC_{61}BM$ or doped $PC_{61}BM$ layer, a significant PL quenching effect was observed (Fig. 3a). This result is consistent with previous studies and can be attributed to the ultrafast charge transfer at the perovskite/fullerene interface.[5] For the undoped $PC_{61}BM$-coated sample, nearly ~ 17% PL intensity was maintained (Fig. 3a). In contrast, almost complete PL intensity was quenched for the sample with a doped $PC_{61}BM$ film (Fig. 3a), suggesting more efficient charge carrier transfer at the perovskite/doped $PC_{61}BM$ interface. This difference is presumably due to the superior film quality of the HMB-doped $PC_{61}BM$ film on the perovskite layer as discussed previously (Fig. 2). Efficient charge transfer was also manifested

31838 | Phys. Chem. Chem. Phys., 2016, 18, 31836–31844

This journal is © the Owner Societies 2016

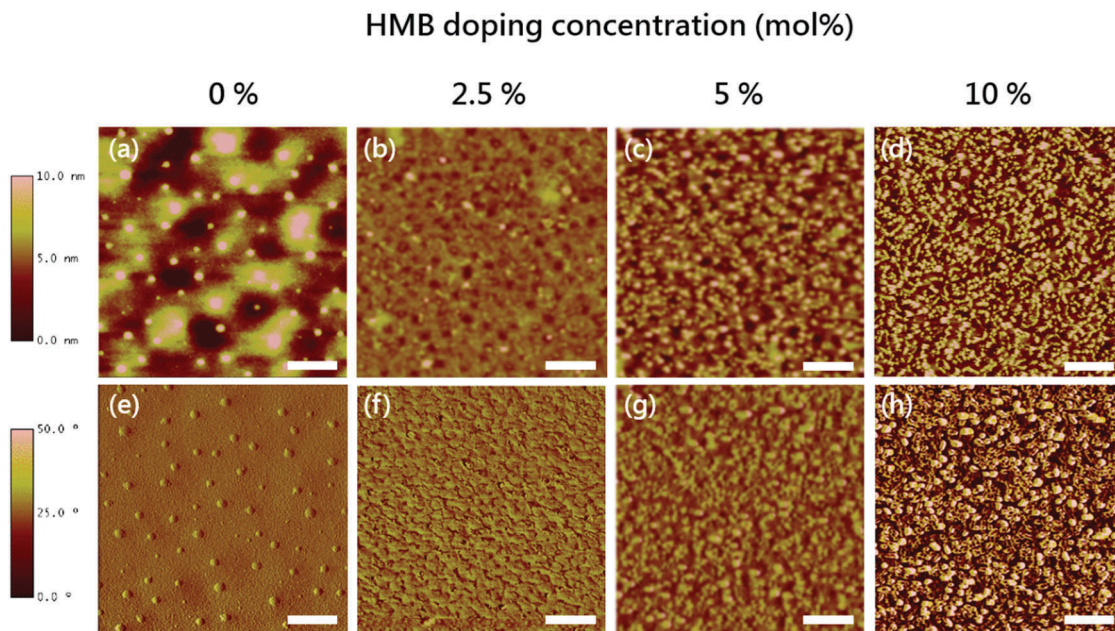## HMB doping concentration (mol%)

Fig. 2   AFM topographical (upper row) and phase (lower row) images of doped $PC_{61}BM$ films at varying dopant concentrations (scale bar = 1 μm).
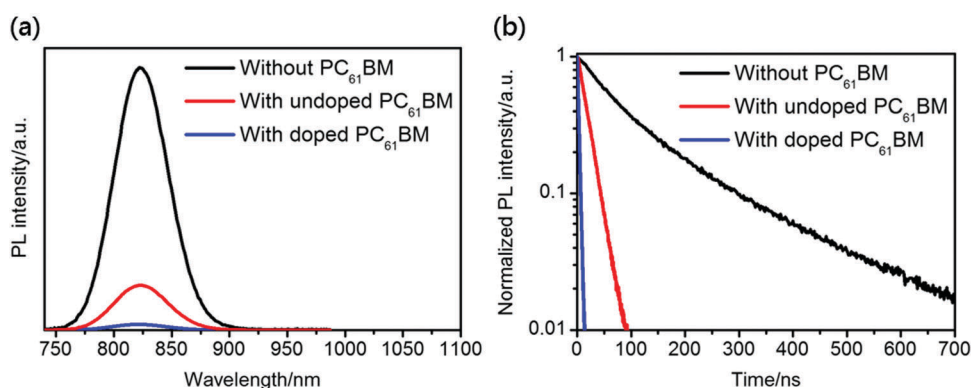

Fig. 3   (a) Steady-state and (b) time-resolved PL spectra of $FAPbI_3$ films with and without $PC_{61}BM$ layers.

in a reduction of the PL lifetimes when the $PC_{61}BM$ layer was present. As shown in Fig. 3b, the pristine $FAPbI_3$ sample showed an average lifetime of 94.3 ns, which is similar to the values reported in the literature studies.[28,29] The average lifetime value extracted for the sample with undoped and doped $PC_{61}BM$ films was 18.9 and 2.8 ns, respectively (Fig. 3b). These results suggest that doping $PC_{61}BM$ with HMB can facilitate the photoinduced charge transfer at the perovskite/$PC_{61}BM$ interface, which in turn can suppress the undesired charge carrier recombination and enhance the charge generation and collection in the devices.

We further examined the effect of doping on the WF of the Ag electrode *via* ultraviolet photoelectron spectroscopy (UPS) measurements. As exhibited in Fig. 4a, the WF value of the bare Ag electrode was determined to be 4.78 eV, which agrees well with the literature values ($\sim$4.70 eV).[30] Considering that the LUMO level of electron-accepting material $PC_{61}BM$ ($\sim$4.10 eV) is lower than the WF of the Ag electrode, this energy level

mismatch can impede the electron extraction from the $PC_{61}BM$ layer to the Ag electrode because of the Schottky-barrier effect, as illustrated in Fig. 4b. When the Ag layer was modified with a doped $PC_{61}BM$ film (5 mol% doping), the WF was significantly reduced to 3.87 eV. The low WF contact at the cathode interface is known to afford good energy level matching with an electron-accepting $PC_{61}BM$ layer and increase the built-in potential of the devices (Fig. 4b), which is beneficial for ensuring efficient electron extraction and producing high open-circuit voltage (V_{oc}) as described previously.[8] Previous studies have shown that the incorporation of cationic surfactants or polyelectrolytes can cause interfacial dipole interaction between the electrode and the active layer and induce a shift in the vacuum level, thereby effectively reducing the WF of the electrode.[8,13–15,31,32] We thus suggest that the positively charged ammonium group on the HMB dopant can form a favorable interfacial dipole between the $PC_{61}BM$ layer and the Ag electrode, leading to a reduction of the WF of the electrode.
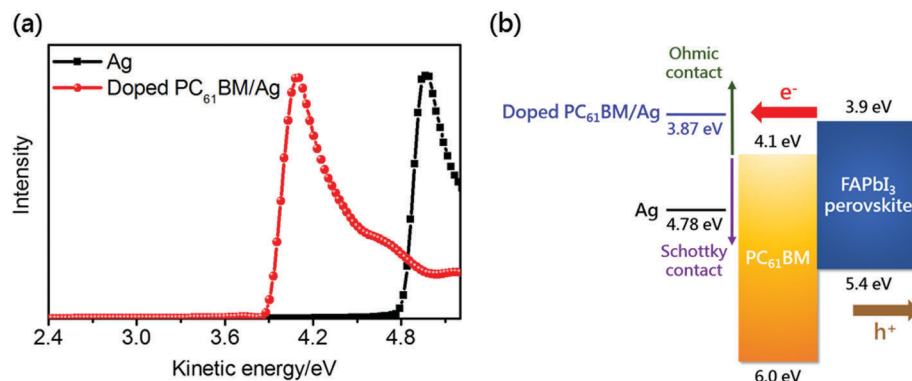
Fig. 4 (a) UPS spectra of bare Ag and modified Ag layers. (b) Energy level diagram at the $PC_{61}BM/Ag$ interface.

The solar-to-electrical PCE of the devices with a HMB-doped $PC_{61}BM$ film (5 mol% doping) was evaluated by recording the current–voltage (J–V) characteristics under simulated AM 1.5 G conditions (intensity = 100 mW cm^{-2}). For comparison, a control device with an undoped $PC_{61}BM$ layer was also prepared. The device configuration used herein was glass substrate/ITO/PEDOT:PSS/FAPbI$_3$/PC$_{61}$BM (with and without HMB doping)/Ag, as illustrated in Fig. 1a. To exclude the possibility of experimental error for the performance evaluation, more than 15 cells for each type of device were fabricated. The average values and the corresponding standard deviations of the photovoltaic parameters including V_{oc}, short-circuit current density (J_{sc}), fill factor (FF), and PCE are summarized in Table 1. The J–V characteristics of the best performing devices are shown in Fig. 5a. For the control devices with an undoped $PC_{61}BM$ layer (device A), a low PCE of 3.23% was attained (Table 1 and Fig. 5a). The poor device performance for device A is consistent with previous findings that the large energy barrier at the $PC_{61}BM/Ag$ interface is present.[8] When applying the HMB-doped $PC_{61}BM$ film as an interfacial layer (device B), a substantial improvement in PCE (by ∼5.6 fold) was observed as a result of the simultaneously increase of all the parameters. The highest PCE we obtained was 17.96%, with a J_{sc} value of 23.89 mA cm^{-2}, a V_{oc} value of 1.04 V, and a FF of 72.34% (Table 1 and Fig. 5a). Note that the measured J_{sc} of device B (23.89 mA cm^{-2}) was reasonably close (within 10% error) to the integrated J_{sc} value obtained from incident photon-to-current conversion efficiency (IPCE) spectra (21.82 mA cm^{-2}; see Fig. 5b). To examine the accuracy of the measured PCE, a steady-state power output at a maximum power point (0.8 V) was measured. Encouragingly, device B exhibited a stabilized power output of 17.6% under continuous illumination (Fig. 5c). The performance improvement observed for device B can be attributed to multi-positive effects afforded by the HMB-doped $PC_{61}BM$ layer, including superior film quality, fine WF tunability of the Ag electrode, and enhanced electrical conductivity, as we have discussed previously. These results clearly indicate the effectiveness of employing the HMB-doped $PC_{61}BM$ film as a promising cathode interfacial layer for PeSCs.

To check the reproducibility of device B, a histogram of device performance obtained from 30 cells is summarized in Fig. 5d, and the narrow PCE distribution was observed. Notably, 80% of the integrated cells showed PCE above 16% with low standard deviation (Table 1 and Fig. 5d), indicating good reproducibility. This can be explained by superior coverage of the HMB-doped $PC_{61}BM$ film on the perovskite layer as depicted in Fig. 2. In addition, considering that planar heterojunction PeSCs have been demonstrated to exhibit an anomalous hysteresis in the J–V curve measurement,[9] the devices with a doped $PC_{61}BM$ layer (device B) measured at different scanning directions and scanning rates were then analyzed. Encouragingly, we observed that our device exhibited photocurrent hysteresis-free J–V characteristics (ESI,† Fig. S2), indicating that the measured PCEs are reliable. The hysteresis-free characteristics of our devices can be ascribed to the effective passivation of trap states in the perovskite afforded by the HMB-doped $PC_{61}BM$ capping layer and/or stable formamidinium cations in the FAPbI$_3$ perovskite structure under the electric field.[33–36]

Controlling the thickness of the $PC_{61}BM$ layer usually plays an important role in performance optimization of PeSCs.[37]

Table 1 Summary of the photovoltaic properties of the devices based on $PC_{61}BM$ interfacial layers (active area = 0.12 cm^2)[a]

Device	Interfacial layer	V_{oc} [volt]	J_{sc} [mA cm^{-2}]	FF [%]	PCE [%]
A[b]	$PC_{61}BM$ (60 nm)	0.45 ± 0.01 (0.45)	16.84 ± 1.09 (18.16)	38.41 ± 3.22 (39.54)	2.92 ± 0.22 (3.23)
B[c]	Doped $PC_{61}BM$ (60 nm)	1.04 ± 0.01 (1.04)	23.01 ± 0.67 (23.89)	69.54 ± 3.76 (72.34)	16.60 ± 0.69 (17.96)
C[b]	$PC_{61}BM$ (90 nm)	0.45 ± 0.01 (0.45)	15.88 ± 0.84 (15.23)	24.15 ± 2.76 (29.37)	1.73 ± 0.20 (2.01)
D[b]	$PC_{61}BM$ (120 nm)	0.45 ± 0.01 (0.49)	12.78 ± 0.67 (13.31)	22.58 ± 1.82 (22.98)	1.31 ± 0.12 (1.50)
E[c]	Doped $PC_{61}BM$ (90 nm)	1.04 ± 0.01 (1.04)	22.87 ± 0.68 (23.02)	67.52 ± 3.53 (71.29)	16.03 ± 0.71 (17.07)
F[c]	Doped $PC_{61}BM$ (120 nm)	1.04 ± 0.01 (1.05)	21.93 ± 0.65 (22.98)	65.35 ± 2.90 (64.60)	14.88 ± 0.48 (15.58)

[a] The values in parentheses are for the best performing devices. [b] Average and standard deviation values were obtained based on 15 devices. [c] Average and standard deviation values were obtained based on 30 devices.
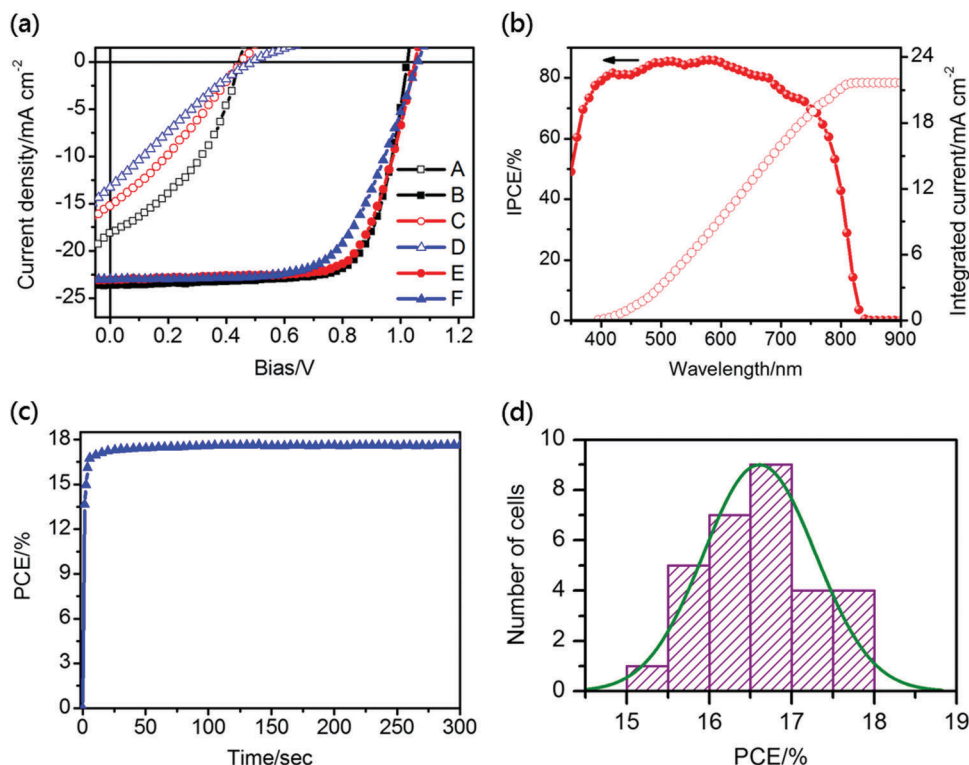
31840 | *Phys. Chem. Chem. Phys.*, 2016, **18**, 31836–31844

This journal is © the Owner Societies 2016

Fig. 5 (a) *J–V* characteristics of the best performing devices based on $PC_{61}BM$ interfacial layers (active area = 0.12 cm^2). (b) IPCE and integrated current spectra of device B. (c) Stabilized power output measured close to the maximum power point (~0.8 V) for device B. (d) Histogram of solar cell efficiencies (device B) for 30 devices.

Here the dependence of device performance on the thickness of the $PC_{61}BM$ film (60–120 nm) was investigated. The film thickness was adjusted by varying the solution concentration (20–45 mg mL^{-1}). For the devices with undoped $PC_{61}BM$ layers, a strong correlation between the performance and the $PC_{61}BM$ film thickness was observed. The PCE rapidly declined from 3.23% to 2.01% when the $PC_{61}BM$ thickness was increased from 60 to 90 nm (Table 1 and Fig. 5a). A further increase in film thickness to 120 nm caused s-shaped kink in the *J–V* characteristics with even a lower PCE of 1.50% (device D; see Table 1 and Fig. 5a), which is generally ascribed to the charge accumulation at the interface.[38] In contrast, for the devices employing a doped film as an interfacial layer, a more slow decline in PCE was observed with respect to the ones with an undoped $PC_{61}BM$ layer (Table 1 and Fig. 5a). The device delivered a reasonable PCE of 15.58% even with a $PC_{61}BM$ film thickness of 120 nm (device F; see Table 1 and Fig. 5a). To the best of our knowledge, this is the highest performance ever reported for PeSCs with a $PC_{61}BM$ thickness more than 100 nm.[37] The thickness-independent performance property could be attributed to the superior electrical conduction property of the HMB-doped $PC_{61}BM$ film, as evidenced by the conductivity measurement shown in Fig. 1c. This property would be beneficial for improving the compatibility of PeSCs with large-area processing techniques. To further demonstrate this concept, we use a scalable blade-coating technique to fabricate large-area (active area = 1.2 cm^2) PeSCs with HMB-doped $PC_{61}BM$ interfacial layers (thickness = 120 nm).

Encouragingly, the devices produced by the blade-coating method (device G) delivered a high PCE up to 15.23%, with a J_{sc} value of 22.35 mA cm^{-2}, a V_{oc} value of 1.05 V, and a FF of 64.90% (Table 2 and Fig. 6a). Very interestingly, the PCEs obtained for the blade-coated devices (device G) were found to be slightly higher than those of the spin-coated devices (device H), as shown in Table 2 and Fig. 6a. This may be associated with the fast drying rate for a blade-coated perovskite layer, which is beneficial for obtaining homogeneous crystallization of a high-quality perovskite film.[39] Further in-depth investigations on the properties of blade-coated films are being carried out to confirm this hypothesis. In addition to the good photovoltaic performance, the stability of the blade-coated devices (device G) was also measured as a function of storage time under an inert nitrogen atmosphere. Obviously, the devices were found to be intrinsically stable, with less than 2% losses in initial PCEs after 1100 hours of storage (Fig. 6b). Good ambient stability was also obtained for the devices encapsulated with epoxy glue and glass slides (ESI,† Fig. S3). These results clearly indicate the high compatibility of HMB-doped $PC_{61}BM$ with scale-up fabrication of high performance PeSCs.

The universality of the HMB dopant was also examined with another fullerene derivative $PC_{71}BM$ (see the ESI,† Fig. S4 for the chemical structure) based on the same processing parameters for each layer as used in the $PC_{61}BM$ system. Compared to $PC_{61}BM$, $PC_{71}BM$ possesses higher optical absorption in visible wavelengths, which is beneficial for the photocurrent

Table 2 Summary of the photovoltaic properties of the spin-coated and blade-coated devices based on 120 nm HMB-doped $PC_{61}BM$ interfacial layers (active area = 1.2 cm^2)[a]

Device	Deposition method	V_{oc} [volt]	J_{sc} [mA cm^{-2}]	FF [%]	PCE [%]
G[b]	Blade coating	1.04 ± 0.01 (1.05)	22.09 ± 0.78 (22.35)	63.83 ± 2.34 (64.90)	14.69 ± 0.46 (15.23)
H[c]	Spin coating	1.04 ± 0.01 (1.05)	21.89 ± 0.64 (22.18)	62.58 ± 2.75 (64.29)	14.24 ± 0.42 (14.97)

[a] The values in parentheses are for the best performing devices. [b] Average and standard deviation values were obtained based on 8 devices. [c] Average and standard deviation values were obtained based on 12 devices.
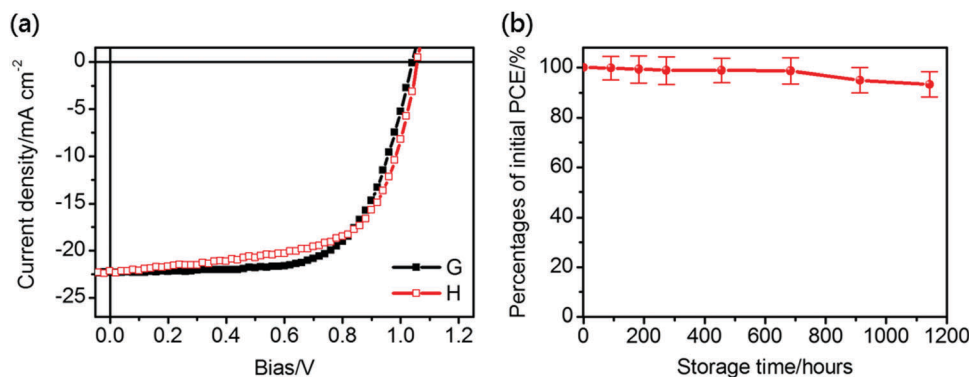
Fig. 6 (a) J–V characteristics of the best performing devices based on $PC_{61}BM$ interfacial layers (active area = 1.2 cm^2). (b) Degradation profile of device G as a function of storage time under an inert nitrogen atmosphere; the statistical data were collected from more than 5 devices.

Table 3 Summary of the photovoltaic properties of the devices based on $PC_{71}BM$ interfacial layers (active area = 0.12 cm^2)[a]

| Device	Interfacial layer	V_{oc} [volt]	J_{sc} [mA cm^{-2}]	FF [%]	PCE [%]
I[b]	Doped $PC_{71}BM$ (60 nm)	1.04 ± 0.01 (1.03)	23.88 ± 0.68 (24.54)	63.08 ± 2.77 (65.77)	15.63 ± 0.51 (16.62)
J[c]	$PC_{71}BM$ (60 nm)	0.45 ± 0.01 (0.43)	16.87 ± 1.10 (18.23)	32.93 ± 4.07 (37.65)	2.49 ± 0.30 (2.95)

[a] The values in parentheses are for the best performing devices. [b] Average and standard deviation values were obtained based on 30 devices. [c] Average and standard deviation values were obtained based on 15 devices.

generation.[40] Encouragingly, the HMB-doped $PC_{71}BM$ layer (60 nm) also presented similar positive effects on the device performance. As shown in Table 3 and Fig. 7, the device with a doped layer (device I) delivered an average PCE of 15.63% (best value = 16.62%), which was much superior to that of the device with an undoped layer (device J). These results provide strong evidence of the general utility of the HMB-doped fullerene film as a viable interfacial layer in PeSCs.

Conclusions

We have demonstrated a facile and effective approach to significantly improve the performance of PeSCs by the incorporation of the HMB-doped $PC_{61}BM$ film as an interfacial layer. This doped interfacial layer delivers several remarkable features for use in PeSCs, including high electrical conductivity, good film coverage on the perovskite layer, efficient interfacial charge transfer ability, appropriate WF tunability of the Ag electrode, and general applicability to different fullerene systems. These characteristics, especially in terms of electrical conductivity, make the PeSCs work well in a wide range of interfacial layer thicknesses (60–120 nm). With these desired properties, the resulting devices deliver a PCE up to ~18%, which contrasts significantly with the PCEs of the devices with undoped $PC_{61}BM$ films (3.2%). Notably, a high PCE of 15.58% is achieved even when a thick HMB-doped $PC_{61}BM$ layer (120 nm) is used, which represents the highest performance ever reported for PeSCs with a
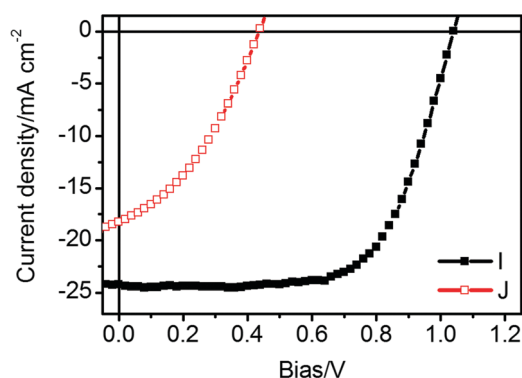
Fig. 7 J–V characteristics of the best performing devices based on $PC_{71}BM$ interfacial layers (active area = 0.12 cm^2).

31842 | *Phys. Chem. Chem. Phys.*, 2016, **18**, 31836–31844

This journal is © the Owner Societies 2016

PC$_{61}$BM thickness more than 100 nm. More encouragingly, a remarkable PCE up to 15.23% is obtained for large-area PeSCs (1.2 cm^2 active area) fabricated by the scalable blade coating technique. Our findings clearly indicate that the HMB-doped fullerene film is a promising candidate as a cathode interfacial layer for PeSCs. The approach demonstrated herein is compatible with up-scalable deposition methods, which can pave the way for the development of large-scale printed PeSC modules. The results may also provide new insights into the development of novel n-doped organic semiconductors for optoelectronic device applications.

Experimental

Materials

Patterned ITO-coated glass substrates (sheet resistance = 15 ohm sq^{-1}) were purchased from Ruilong Tech. HMB was purchased from Sigma-Aldrich. PEDOT:PSS (CLEVIOS P VP Al 4083) was purchased from Heraeus. Formamidinium iodide (FAI; >99.5%) was purchased from Lumtec. PC$_{61}$BM (>99.5%) and PC$_{71}$BM (>99.5%) were purchased from Solenne. The lead iodide (PbI$_2$) complex was prepared according to the previously reported method.[35] In detail, 25 g of PbI$_2$ was dissolved in 75 mL of anhydrous dimethyl sulfoxide. The mixture was then stirred at room temperature for 3 hours, followed by the addition of 200 mL of toluene. The white precipitation was then filtered and dried in a vacuum oven at 60 °C for 12 hours.

Solar cell fabrication

ITO-coated glass substrates were first ultrasonicated in detergent, deionized water, acetone and 2-propanol in turn, followed by UV-ozone treatment for 60 min. After filtration through a 0.45 μm filter, the PEDOT:PSS layer (30 nm) was spin-coated on the cleaned ITO substrate at 4000 rpm for 60 s and then annealed at 120 °C for 15 min. The substrates were then transferred to a nitrogen-filled glovebox. For the spin-coated devices, the FAPbI$_3$ perovskite layer (~320 nm) was prepared according to the reported procedure.[35] Briefly, the solution of the PbI$_2$ complex in anhydrous dimethylformamide with a concentration of 1.3 M was spin-coated at 3000 rpm for 30 s. Afterward, the solution of FAI in anhydrous 2-propanol with a concentration of 0.465 M was spin-coated on top of the PbI$_2$ film at 5000 rpm for 30 s and then annealed at 150 °C for 10 min. After the deposition of the perovskite layer, the solution of PC$_{61}$BM or PC$_{71}$BM in anhydrous chloroform was spin-coated on top of the perovskite layers at 1000 rpm for 60 s. For the blade-coated devices, 15 μL of PbI$_2$ complex solution (1.1 M in anhydrous dimethylformamide) was dispensed from a syringe under the edge of the blade fixed at 100 μm above the substrate surface, and the blade was dragged at a constant speed of 70 mm s^{-1}. It should be noted that the substrates were heated at an elevated temperature of 80 °C during the blade deposition in order to obtain a compact film with good uniformity. FAPbI$_3$ crystallization was achieved by dipping the PbI$_2$-coated samples into the FAI solution (20 mg mL^{-1} in anhydrous 2-propanol). The as-deposited perovskite films were subsequently thermally annealed at 150 °C for 10 min. 10 μL of the PC$_{61}$BM solution (30 mg in anhydrous 2-CP) was then dropped onto the preheated covered substrates (110 °C) and swiped linearly by a blade with a constant speed of 10 mm s^{-1}. The gap between the blade and the substrate was fixed at 300 μm. Ag (150 nm) was then deposited from a thermal evaporator under high vacuum (<10^{-6} Torr). Finally, all the fabricated devices were encapsulated with glass coverslips and UV-curable epoxy resin. To eliminate the J_{sc} from regions outside the active area, illumination masks with an aperture size of 0.12 cm^2 or 1.2 cm^2 were used.

Characterization

For the evaluation of the device performance, the devices were illuminated at a light intensity of 100 mW cm^{-2} by using a 150 W Class AAA solar simulator (XES-100S1, SAN-EI). The light intensity was determined by using a standard silicon photodiode (Hamamatsu S1133) calibrated by the National Renewable Energy Laboratory. The current–voltage curves were recorded using a Keithley 2400 digital source meter. Unless otherwise stated, the scan rate was set at 0.15 V s^{-1}. The IPCE spectra were recorded using a lock-in amplifier coupled with a monochromator with a 250 W quartz-halogen lamp (Osram). The work functions of the electrodes were measured using a ULVAC-PHI PHI 5000 Versaprobe II X-ray photoelectron spectrometer employing a mono-chromatic focused Al-Kα X-ray source and a hemispherical analyzer. The EPR spectra were recorded at room temperature using a Bruker ELEXSYS E-580 EPR spectrometer. Steady-state PL spectra were recorded at room temperature using a fluorescence spectrophotometer (Hitachi F-4600). Time-resolved PL decay spectra were obtained on a time-correlated single-photon counting system (Edinburgh Instruments FL920) using a 530 nm excitation source and the emission was monitored at 770 nm. The lifetimes were calculated by fitting the experimental PL decay transients to the single-exponential decay model. The AFM images were characterized using a Digital Instrument D3100CL.

Acknowledgements

Notes and references

1 M. Liu, M. B. Johnston and H. J. Snaith, *Nature*, 2013, **501**, 395–398.
2 P. Gao, M. Gratzel and M. K. Nazeeruddin, *Energy Environ. Sci.*, 2014, **7**, 2448–2463.
3 M. Saliba, T. Matsui, J.-Y. Seo, K. Domanski, J.-P. Correa-Baena, M. K. Nazeeruddin, S. M. Zakeeruddin, W. Tress, A. Abate, A. Hagfeldt and M. Gratzel, *Energy Environ. Sci.*, 2016, **9**, 1989–1997.
4 H. S. Jung and N.-G. Park, *Small*, 2015, **11**, 10–25.

This journal is © the Owner Societies 2016

Phys. Chem. Chem. Phys., 2016, **18**, 31836–31844 | **31843**

5 T. Liu, K. Chen, Q. Hu, R. Zhu and Q. Gong, *Adv. Energy Mater.*, 2016, DOI: 10.1002/aenm.201600457.

6 O. Malinkiewicz, A. Yella, Y. H. Lee, G. M. Espallargas, M. Graetzel, M. K. Nazeeruddin and H. J. Bolink, *Nat. Photonics*, 2014, **8**, 128–132.

7 H. Zhou, Q. Chen, G. Li, S. Luo, T.-b. Song, H.-S. Duan, Z. Hong, J. You, Y. Liu and Y. Yang, *Science*, 2014, **345**, 542–546.

8 C.-C. Chueh, C.-Z. Li and A. K. Y. Jen, *Energy Environ. Sci.*, 2015, **8**, 1160–1189.

9 R. Fan, Y. Huang, L. Wang, L. Li, G. Zheng and H. Zhou, *Adv. Energy Mater.*, 2016, DOI: 10.1002/aenm.201600460.

10 L. Meng, J. You, T.-F. Guo and Y. Yang, *Acc. Chem. Res.*, 2016, **49**, 155–165.

11 A. Guerrero, J. You, C. Aranda, Y. S. Kang, G. Garcia-Belmonte, H. Zhou, J. Bisquert and Y. Yang, *ACS Nano*, 2016, **10**, 218–224.

12 T. A. Berhe, W.-N. Su, C.-H. Chen, C.-J. Pan, J.-H. Cheng, H.-M. Chen, M.-C. Tsai, L.-Y. Chen, A. A. Dubale and B.-J. Hwang, *Energy Environ. Sci.*, 2016, **9**, 323–356.

13 H. Zhang, H. Azimi, Y. Hou, T. Ameri, T. Przybilla, E. Spiecker, M. Kraft, U. Scherf and C. J. Brabec, *Chem. Mater.*, 2014, **26**, 5190–5193.

14 J. Min, Z.-G. Zhang, Y. Hou, C. O. Ramirez Quiroz, T. Przybilla, C. Bronnbauer, F. Guo, K. Forberich, H. Azimi, T. Ameri, E. Spiecker, Y. Li and C. J. Brabec, *Chem. Mater.*, 2015, **27**, 227–234.

15 C.-Y. Chang, Y.-C. Chang, W.-K. Huang, K.-T. Lee, A.-C. Cho and C.-C. Hsu, *Chem. Mater.*, 2015, **27**, 7119–7127.

16 F. X. Xie, D. Zhang, H. Su, X. Ren, K. S. Wong, M. Grätzel and W. C. H. Choy, *ACS Nano*, 2015, **9**, 639–646.

17 C.-Y. Chang, K.-T. Lee, W.-K. Huang, H.-Y. Siao and Y.-C. Chang, *Chem. Mater.*, 2015, **27**, 5122–5130.

18 C.-Y. Chang, W.-K. Huang, Y.-C. Chang, K.-T. Lee and C.-T. Chen, *J. Mater. Chem. A*, 2016, **4**, 640–648.

19 C.-Y. Chang, W.-K. Huang, J.-L. Wu, Y.-C. Chang, K.-T. Lee and C.-T. Chen, *Chem. Mater.*, 2016, **28**, 242–251.

20 C.-Y. Chang, Y.-C. Chang, W.-K. Huang, W.-C. Liao, H. Wang, C. Yeh, B.-C. Tsai, Y.-C. Huang and C.-S. Tsao, *J. Mater. Chem. A*, 2016, **4**, 7903–7913.

21 P.-W. Liang, C.-Y. Liao, C.-C. Chueh, F. Zuo, S. T. Williams, X.-K. Xin, J. Lin and A. K. Y. Jen, *Adv. Mater.*, 2014, **26**, 3748–3754.

22 Z. Zhu, Q. Xue, H. He, K. Jiang, Z. Hu, Y. Bai, T. Zhang, S. Xiao, K. Gundogdu, B. R. Gautam, H. Ade, F. Huang, K. S. Wong, H.-L. Yip, S. Yang and H. Yan, *Adv. Sci.*, 2015, DOI: 10.1002/advs.201500353.

23 S.-I. Na, S.-S. Kim, J. Jo and D.-Y. Kim, *Adv. Mater.*, 2008, **20**, 4061–4067.

24 H. Zhou, Y. Zhang, C.-K. Mai, S. D. Collins, T.-Q. Nguyen, G. C. Bazan and A. J. Heeger, *Adv. Mater.*, 2014, **26**, 780–785.

25 C.-Z. Li, C.-C. Chueh, F. Ding, H.-L. Yip, P.-W. Liang, X. Li and A. K. Y. Jen, *Adv. Mater.*, 2013, **25**, 4425–4430.

26 C.-Z. Li, C.-C. Chueh, H.-L. Yip, F. Ding, X. Li and A. K. Y. Jen, *Adv. Mater.*, 2013, **25**, 2457–2461.

27 C.-Y. Chang, W.-K. Huang and Y.-C. Chang, *Chem. Mater.*, 2016, **28**, 6305–6312.

28 D.-X. Yuan, A. Gorka, M.-F. Xu, Z.-K. Wang and L.-S. Liao, *Phys. Chem. Chem. Phys.*, 2015, **17**, 19745–19750.

29 G. E. Eperon, S. D. Stranks, C. Menelaou, M. B. Johnston, L. M. Herz and H. J. Snaith, *Energy Environ. Sci.*, 2014, **7**, 982–988.

30 J.-P. Hong, A.-Y. Park, S. Lee, J. Kang, N. Shin and D. Y. Yoon, *Appl. Phys. Lett.*, 2008, **92**, 143311.

31 S.-H. Oh, S.-I. Na, J. Jo, B. Lim, D. Vak and D.-Y. Kim, *Adv. Funct. Mater.*, 2010, **20**, 1977–1983.

32 B. H. Lee, I. H. Jung, H. Y. Woo, H.-K. Shim, G. Kim and K. Lee, *Adv. Funct. Mater.*, 2014, **24**, 1100–1108.

33 Q. Wang, Y. Shao, Q. Dong, Z. Xiao, Y. Yuan and J. Huang, *Energy Environ. Sci.*, 2014, **7**, 2359–2365.

34 Y. Shao, Z. Xiao, C. Bi, Y. Yuan and J. Huang, *Nat. Commun.*, 2014, **5**, 5784.

35 W. S. Yang, J. H. Noh, N. J. Jeon, Y. C. Kim, S. Ryu, J. Seo and S. I. Seok, *Science*, 2015, **348**, 1234–1237.

36 J.-W. Lee, D.-J. Seol, A.-N. Cho and N.-G. Park, *Adv. Mater.*, 2014, **26**, 4991–4998.

37 J. Seo, S. Park, Y. Chan Kim, N. J. Jeon, J. H. Noh, S. C. Yoon and S. I. Seok, *Energy Environ. Sci.*, 2014, **7**, 2642–2646.

38 J. C. Wang, X. C. Ren, S. Q. Shi, C. W. Leung and P. K. L. Chan, *Org. Electron.*, 2011, **12**, 880–885.

39 Y. Deng, E. Peng, Y. Shao, Z. Xiao, Q. Dong and J. Huang, *Energy Environ. Sci.*, 2015, **8**, 1544–1550.

40 M. M. Wienk, J. M. Kroon, W. J. H. Verhees, J. Knol, J. C. Hummelen, P. A. van Hal and R. A. J. Janssen, *Angew. Chem., Int. Ed.*, 2003, **42**, 3371–3375.